Iterative Adaptive Approach for Wide-band Active Sonar Array Processing

Zhaofu Chen*, Jian Li†, *Fellow*, *IEEE*, Petre Stoica‡, *Fellow*, *IEEE* and Kam W. Lo§, *Senior Member*, *IEEE*
*Department of Electrical and Computer Engineering
University of Florida, Gainesville, Florida, USA, 32611
Phone: 1-352-328-6474; Email: cgcruiser@ufl.edu
†Department of Electrical and Computer Engineering
University of Florida, Gainesville, Florida, USA, 32611
Phone: 1-352-392-2642; Fax: 1-352-392-0044; Email: li@dsp.ufl.edu
‡Department of Information Technology
Uppsala University, Uppsala, Sweden
Phone: 46-18-471.7619; Fax: 46-18-511925; Email: peter.stoica@it.uu.se
§Maritime Operations Division
Defence Science & Technology Organization, Eveleigh NSW 2015, Australia
Email: kam.lo@dsto.defence.gov.au

***Abstract*— Sector scan sonars can be used for detection and identification of man-made objects located on the sea floor. Wide-band acoustic signals are employed in this kind of sonar system to enhance range resolution. The conventional delay-and-sum beamformer (CBF) produces sonar images with high sidelobe levels and poor angular resolution. Adaptive beamforming algorithms together with spatial resampling can be applied to mitigate this problem. The algorithm "Spatial Processing: Optimized and Constrained" (SPOC), used in a recent work, is studied herein and shown to be identical to the basic form of the FOCal Underdetermined System Solver (FOCUSS) algorithm. A recently developed algorithm, the Iterative Adaptive Approach (IAA), is proposed for this sonar application and various implementation issues are discussed. Experimental results show that the IAA algorithm produces better sonar images than the CBF and Minimum Variance Distortionless Response (MVDR) algorithms in terms of sidelobe suppression and angular resolution. Compared with SPOC, IAA provides clearer acoustic highlights of the imaged object and a higher density of pixels representing the object.**

I. Introduction

A high-frequency sector scan sonar can be used to detect and identify man-made objects located on the sea floor [1] [2] [3] [4] [5]. Typically, such a sonar system consists of a transmitter (projector) that emits an acoustic pulse toward the targeted region and a horizontal linear array of sensors (hydrophones) that receive the echoes reflected back from the region. The returned signal at each sensor bears information on the targets inside the region and can be processed to produce a two-dimensional (range and angle) sonar image capturing the acoustic highlights of the objects. Two aspects deserve our attention when we consider the sonar imaging problem once the operating frequency is fixed. First, the range resolution is inversely proportional to the bandwidth B of the transmitted acoustic signal. Therefore, a wide-band sonar system is naturally preferred for its better range resolution. Second, the angular resolution $\Delta\theta$ is closely related to the aperture size L_a of the sensor array. When the conventional data-independent delay-and-sum beamformer (CBF) is used to generate a sonar image, we have $\Delta\theta \propto \frac{1}{L_a}$, so the angular resolution is limited by the aperture size of the array. Adaptive beamformers have the potential of improving the angular resolution for a given L_a. However, previous work on adaptive beamformers for active sonars assumes narrow-band signals and is therefore inapplicable to wide-band systems. Recently [6], the method of spatial resampling (see [7] for details on this technique) was proposed to eliminate the frequency dependency in the sensor signal model for a wide-band active sonar. The resulting sensor data can then be processed with existing narrow-band adaptive beamforming (or high-resolution angular spectral estimation) techniques.

Another challenge emerges when the number of snapshots (pings) available for image formation is limited. This occurs, for example, when the sonar platform is an autonomous underwater vehicle (AUV). Due to the motion of the AUV and the highly non-stationary nature of the underwater environment, only single snapshot adaptive algorithms can be directly used. For the algorithms that require the array covariance matrix, spatial smoothing can be used to estimate the matrix from a single snapshot by forming overlapping subarrays at the cost of angular resolution, provided that the receive array is a uniform linear array (ULA). In [6] the CBF and three adaptive algorithms, namely MUltiple SIgnal Classification (MUSIC), Minimum Variance Distortionless Response (MVDR) and Spatial Processing: Optimized and Constrained (SPOC) [8] were considered and their performances evaluated using real sonar data. Both MUSIC and MVDR were used with spatial smoothing. It was shown that the adaptive algorithms outperform the CBF in terms of sidelobe suppression and angular resolution.

In this paper, the SPOC algorithm is shown to be identical to the basic form of another adaptive algorithm known as the FOCal Underdetermined System Solver (FOCUSS) [9]. As a

978-1-4244-5222-4/10/$26.00 ©2010 IEEE

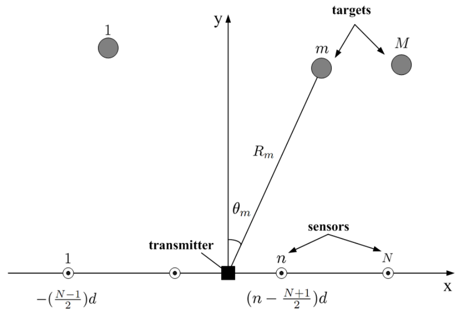

Fig. 1. Schematics of the hydrophone array.

result, SPOC can be evaluated based on the knowledge of the performance of FOCUSS [9] [10]. Furthermore, a recently developed algorithm called the Iterative Adaptive Approach (IAA) [10] is introduced for the wide-band active sonar application. Various aspects pertaining to implementation details of IAA including regularizations and computational complexities are discussed. The IAA algorithm is applied to real sonar data and its performance is evaluated by comparing the IAA images with those generated using the CBF, MVDR and SPOC algorithms.

The rest of this paper is organized as follows. Section II describes the sonar-transmitter configuration and sensor signal model for the wide-band active sonar. Section III describes the various adaptive beamforming algorithms (SPOC, MVDR and IAA), with special focus on the IAA algorithm. A mathematical derivation is included to show that SPOC is identical to the basic form of FOCUSS. Section IV presents the experimental results and compares the performances of the CBF and various adaptive beamforming algorithms. Finally the paper is concluded in Section V.

II. Preliminaries and the Signal Model

Figure 1 shows a linear hydrophone array with N sensors uniformly placed along the x axis with an interelement spacing d. The Cartesian coordinate system is chosen so that the origin coincides with the center of the array, and the y axis points along the broadside direction. The coordinate of hydrophone n is given by $(x_n, y_n) = ((n - \frac{N+1}{2})d, 0)$ for $1 \le n \le N$. A projector shown as the filled square is located at the array center. M far-field point targets, with their locations given by the polar coordinates (R_m, θ_m) for $1 \le m \le M$, are denoted by the gray circles.

The projector emits a wide-band pulse

$$p(t) = b(t)\exp(j2\pi f_c t), \tag{1}$$

where $b(t)$ is the complex envelope with a bandwidth B and f_c is the carrier frequency. The received signal at hydrophone n can be expressed as the sum of M delayed versions of $p(t)$, with their amplitudes modified by the backscattering coefficients of the M targets. The received signal at each hydrophone is demodulated into baseband followed by matched filtering. The complex baseband matched filtered output signal of hydrophone n can be expressed as:

$$z_n(t) = \sum_{m=1}^{M} \rho_m a(t-\tau_{nm}) e^{-j2\pi f_c \tau_{nm}} + \epsilon_n(t), \quad 1 \le n \le N, \tag{2}$$

where ρ_m is the backscattering coefficient of target m, $a(t)$ is the autocorrelation function of $b(t)$, $\epsilon_n(t)$ accounts for ambient noises and reverberations, and τ_{nm} is the time needed for the pulse to reach target m and then return to sensor n. Under the assumption that the M targets are located in the far field of the array, the returned echoes incident onto the array can be regarded as plane waves. As such, τ_{nm} can be expressed as:

$$\tau_{nm} = \frac{2R_m - x_n \sin\theta_m}{c}, \tag{3}$$

where c is the underwater sound speed. Substituting this expression into (2) and taking the Fourier transform of (2) gives:

$$Z_n(f) = \sum_{m=1}^{M} \alpha_m A(f) e^{-j\frac{4\pi f R_m}{c}} e^{j\frac{2\pi(f+f_c)x_n \sin\theta_m}{c}} + E_n(f), \quad 1 \le n \le N, \tag{4}$$

where $\alpha_m = \rho_m e^{-j4\pi f_c R_m/c}$ and $A(f)$ is the Fourier transform of $a(t)$. Here $Z_n(f)$ can be interpreted as a sample of a noisy acoustic field at (f, x_n). However, the second exponential term on the right hand side of (4) depends on both frequency f and hydrophone location x_n, and hence narrow-band adaptive array processing algorithms cannot be applied directly. The frequency dependence of this term can be eliminated using spatial resampling. The noisy acoustic field is resampled (or interpolated) at $(f, \tilde{x}_n)$, where

$$\tilde{x}_n = \frac{f_c - B/2}{f + f_c} x_n, \quad 1 \le n \le N \tag{5}$$

and for each frequency f satisfying $|f| \le B/2$ using the available samples $\{Z_n(f) : 1 \le n \le N\}$ [6]. An example of a suitable resampling method is the cubic interpolation technique [7].

Denote the resampled data as $\{\tilde{Z}_n(f) : 1 \le n \le N\}$. Substituting the expression for $\tilde{x}_n$ into (4) gives:

$$\tilde{Z}_n(f) = \sum_{m=1}^{M} \beta_m A(f) e^{-j\frac{4\pi f R_m}{c}} e^{j(n-1)\phi_m} + \tilde{E}_n(f), \quad 1 \le n \le N, \tag{6}$$

where $\phi_m = \pi(2f_c - B)d\sin\theta_m/c$, $\beta_m = \alpha_m e^{-j(N-1)\phi_m/2}$ and $\tilde{E}_n(f)$ represents the resampled noise field at $(f, \hat{x}_n)$.

III. Adaptive Beamforming

Taking the inverse Fourier transform of $\tilde{Z}_n(f)$ yields:

$$\tilde{z}_n(t) = \sum_{m=1}^{M} \beta_m a(t - 2R_m/c) e^{j(n-1)\phi_m} + \tilde{\epsilon}_n(t), \quad 1 \le n \le N, \tag{7}$$

where $\tilde{z}_n(t)$ and $\tilde{\epsilon}_n(t)$ are the inverse Fourier transforms of $\tilde{Z}_n(f)$ and $\tilde{E}_n(f)$, respectively. Since the autocorrelation function $a(t)$ peaks at $t = 0$, the magnitude of $\tilde{z}_n(t)$ will have M maximal points located at $t = 2R_m/c$, $1 \leq m \leq M$, corresponding to the ranges of the M targets (assuming sufficient range separations of the targets). We then estimate the angular spectrum for each value of t using the resampled hydrophone data $\tilde{z}_n(t)$, $1 \leq n \leq N$. This produces a sonar image in the polar coordinate system (R, θ), where $R = ct/2$ is the range measured from the center of the array and θ is the bearing measured with respect to the broadside direction of the array. Since the data model in (7) is similar to the plane wave model for narrow-band array processing, existing high-resolution beamforming techniques can be applied to estimate the angular spectra [6].

A. Spatial Processing: Optimized and Constrained (SPOC)

SPOC [6] [8] is a single-snapshot processing algorithm that maximizes the *a posteriori* data probability density function to obtain a constrained optimization solution. For each range bin, this algorithm assumes the presence of a large number of potential targets uniformly located on a fine grid with $K \gg N$ points in it. Since the angular estimations for different range bins are independent of each other, we drop the dependence of various quantities on t for notational simplicity. (The sampling interval between range bins should be no greater than the sonar range resolution, which is inversely proportional to the sonar bandwidth B.)

To introduce the SPOC algorithm, we denote the bearing and power of the kth target (i.e., the target at the kth grid point) as $\tilde{\theta}_k$ and $|s_k(t)|^2$, respectively. The algorithm estimates the target strengths at all grid points, and the peaks in the so-obtained spectrum are considered to be associated with the true targets. By defining $\tilde{\mathbf{z}} = [\tilde{z}_1, \cdots, \tilde{z}_N]^{\mathrm{T}}$ to be the $N \times 1$ resampled sensor signal vector, $\mathbf{s} = [s_1, \cdots, s_K]^{\mathrm{T}}$ to be the $K \times 1$ target strength vector, and $\mathbf{a}_k = [1, e^{j\tilde{\phi}_k}, \cdots, e^{j(N-1)\tilde{\phi}_k}]^{\mathrm{T}}$ to be the $N \times 1$ array steering vector, where $\tilde{\phi}_k = \pi(2f_c - B)d \sin \tilde{\theta}_k / c$, the resampled hydrophone output data model can be compactly expressed in matrix form as:

$$\tilde{\mathbf{z}} = \sum_{k=1}^{K} \mathbf{a}_k s_k = \mathbf{A}\mathbf{s}, \tag{8}$$

where $\mathbf{A} = [\mathbf{a}_1, \cdots, \mathbf{a}_K]$ is the $N \times K$ array steering matrix.

The SPOC algorithm solves the maximum *a posteriori* estimation problem under the constraint that the data model in (8) holds. Mathematically, SPOC seeks the solution to the following optimization problem:

$$\begin{aligned} \min \quad & \sum_{k=1}^{K} \ln |s_k|^2 \\ \text{s.t.} \quad & \tilde{\mathbf{z}} = \mathbf{A}\mathbf{s} \,. \end{aligned} \tag{9}$$

To solve this problem, SPOC adopts a parameter representation model by decomposing the unknown target vector $\mathbf{s}$ into a vector of fixed parameters and another vector of free parameters. The vector of fixed parameters is used to satisfy the constraint, while the vector of free parameters is chosen in such a way that the cost function in (9) is minimized. The angular spectral estimate $|\hat{s}_k|^2$ at each angle $\tilde{\theta}_k$, for $1 \leq k \leq K$, can be computed using the following equation [6] [8]:

$$\begin{aligned} \hat{\mathbf{s}} = &\mathbf{V}\boldsymbol{\Lambda}^{-1}\mathbf{V}^{\mathrm{H}}\mathbf{A}^{\mathrm{H}}\tilde{\mathbf{z}} \\ &+ \tilde{\mathbf{V}}(\tilde{\mathbf{V}}^{\mathrm{H}}\mathbf{P}\mathbf{V})(\mathbf{V}^{\mathrm{H}}\mathbf{P}\mathbf{V})^{-1}\boldsymbol{\Lambda}^{-1}\mathbf{V}^{\mathrm{H}}\mathbf{A}^{\mathrm{H}}\tilde{\mathbf{z}}, \end{aligned} \tag{10}$$

where $\hat{\mathbf{s}} = [\hat{s}_1, \cdots, \hat{s}_K]^T$, $\mathbf{P} = \mathrm{diag}(|\hat{s}_1|^2, \cdots, |\hat{s}_K|^2)$ and the matrices $\mathbf{V}$, $\tilde{\mathbf{V}}$ and $\boldsymbol{\Lambda}$ (of dimensions $K \times N$, $K \times (K-N)$ and $N \times N$, respectively) are defined by the eigen-decomposition of $\mathbf{A}^{\mathrm{H}}\mathbf{A}$ as follows:

$$\mathbf{A}^{\mathrm{H}}\mathbf{A} = \begin{bmatrix} \mathbf{V} & \tilde{\mathbf{V}} \end{bmatrix} \begin{bmatrix} \boldsymbol{\Lambda} & \mathbf{0} \\ \mathbf{0} & \mathbf{0} \end{bmatrix} \begin{bmatrix} \mathbf{V}^{\mathrm{H}} \\ \tilde{\mathbf{V}}^{\mathrm{H}} \end{bmatrix} = \mathbf{V}\boldsymbol{\Lambda}\mathbf{V}^{\mathrm{H}} \,. \tag{11}$$

Since the matrix $\mathbf{A}$ is of dimension $N \times K$, where $N \ll K$, the matrix $\mathbf{A}^{\mathrm{H}}\mathbf{A}$ is at most of rank N. If the K grid points $\tilde{\theta}_k$, $1 \leq k \leq K$, span only a small range of angles, then not all the column vectors in $\mathbf{A}$ will be linearly independent and hence the rank of $\mathbf{A}^{\mathrm{H}}\mathbf{A}$ will be smaller than N. However, in our application where $\tilde{\theta}_k \in (-90°, 90°)$, the rank of $\mathbf{A}^{\mathrm{H}}\mathbf{A}$ is N, so $\boldsymbol{\Lambda}$ is generally a diagonal matrix with the N non-zero eigenvalues of $\mathbf{A}^{\mathrm{H}}\mathbf{A}$ on its diagonal.

Since the matrix $\mathbf{P}$ contains the unknowns $\{|\hat{s}_k|^2\}_{k=1}^{K}$, the SPOC algorithm has to be implemented in an iterative manner, in which $\mathbf{P}$ is constructed from the estimates obtained from the previous iteration. To initialize SPOC using the parameter representation model, the vector of fixed parameters is chosen to satisfy the constraint while the vector of free parameters is set to zero. Specifically, the initial estimate $\hat{\mathbf{s}}^{(0)}$ is calculated as:

$$\hat{\mathbf{s}}^{(0)} = \mathbf{V}\boldsymbol{\Lambda}^{-1}\mathbf{V}^{\mathrm{H}}\mathbf{A}^{\mathrm{H}}\tilde{\mathbf{z}} \,. \tag{12}$$

We note that this corresponds to the first term in (10), which is formed from the fixed parameters. Therefore, in each subsequent iteration, only the second term in (10) that corresponds to the free parameters needs to be updated.

Employing matrix operations, we can rewrite the expression in (10) as follows:

$$\begin{aligned} \hat{\mathbf{s}} &= [\mathbf{V} + \tilde{\mathbf{V}}(\tilde{\mathbf{V}}^{\mathrm{H}}\mathbf{P}\mathbf{V})(\mathbf{V}^{\mathrm{H}}\mathbf{P}\mathbf{V})^{-1}]\boldsymbol{\Lambda}^{-1}\mathbf{V}^{\mathrm{H}}\mathbf{A}^{\mathrm{H}}\tilde{\mathbf{z}} \\ &= (\mathbf{V}\mathbf{V}^{\mathrm{H}}\mathbf{P}\mathbf{V} + \tilde{\mathbf{V}}\tilde{\mathbf{V}}^{\mathrm{H}}\mathbf{P}\mathbf{V})(\mathbf{V}^{\mathrm{H}}\mathbf{P}\mathbf{V})^{-1}\boldsymbol{\Lambda}^{-1}\mathbf{V}^{\mathrm{H}}\mathbf{A}^{\mathrm{H}}\tilde{\mathbf{z}} \\ &= (\mathbf{V}\mathbf{V}^{\mathrm{H}} + \tilde{\mathbf{V}}\tilde{\mathbf{V}}^{\mathrm{H}})\mathbf{P}\mathbf{V}(\mathbf{V}^{\mathrm{H}}\mathbf{P}\mathbf{V})^{-1}\boldsymbol{\Lambda}^{-1}\mathbf{V}^{\mathrm{H}}\mathbf{A}^{\mathrm{H}}\tilde{\mathbf{z}} \\ &= \mathbf{P}\mathbf{V}(\mathbf{V}^{\mathrm{H}}\mathbf{P}\mathbf{V})^{-1}\boldsymbol{\Lambda}^{-1}\mathbf{V}^{\mathrm{H}}\mathbf{A}^{\mathrm{H}}\tilde{\mathbf{z}} \,. \end{aligned} \tag{13}$$

From (11), $\mathbf{A} = \mathbf{U}\boldsymbol{\Lambda}^{\frac{1}{2}}\mathbf{V}^{\mathrm{H}}$, where $\mathbf{U}$ is an $N \times N$ unitary matrix such that $\mathbf{U}^{\mathrm{H}}\mathbf{U} = \mathbf{I}$. Note that we can further rewrite (13) as follows:

$$\begin{aligned} \hat{\mathbf{s}} = &\mathbf{P}\mathbf{V}(\boldsymbol{\Lambda}^{\frac{1}{2}}\mathbf{U}^{\mathrm{H}})(\boldsymbol{\Lambda}^{\frac{1}{2}}\mathbf{U}^{\mathrm{H}})^{-1}(\mathbf{V}^{\mathrm{H}}\mathbf{P}\mathbf{V})^{-1} \\ &(\mathbf{U}\boldsymbol{\Lambda}^{\frac{1}{2}})^{-1}(\mathbf{U}\boldsymbol{\Lambda}^{\frac{1}{2}})\boldsymbol{\Lambda}^{-1}\mathbf{V}^{\mathrm{H}}\mathbf{A}^{\mathrm{H}}\tilde{\mathbf{z}} \\ = &\mathbf{P}\mathbf{V}\boldsymbol{\Lambda}^{\frac{1}{2}}\mathbf{U}^{\mathrm{H}}(\mathbf{U}\boldsymbol{\Lambda}^{\frac{1}{2}}\mathbf{V}^{\mathrm{H}}\mathbf{P}\mathbf{V}\boldsymbol{\Lambda}^{\frac{1}{2}}\mathbf{U}^{\mathrm{H}})^{-1} \\ &\mathbf{U}\boldsymbol{\Lambda}^{-\frac{1}{2}}\mathbf{V}^{\mathrm{H}}\mathbf{V}\boldsymbol{\Lambda}^{\frac{1}{2}}\mathbf{U}^{\mathrm{H}}\tilde{\mathbf{z}} \,. \end{aligned} \tag{14}$$

Substituting $\mathbf{A} = \mathbf{U}\boldsymbol{\Lambda}^{\frac{1}{2}}\mathbf{V}^{\mathrm{H}}$ into (14) and making use of the fact that $\mathbf{V}^{\mathrm{H}}\mathbf{V} = \mathbf{I}$, the angular spectral estimate can be expressed as:

$$\hat{\mathbf{s}} = \mathbf{P}\mathbf{A}^{\mathrm{H}}(\mathbf{A}\mathbf{P}\mathbf{A}^{\mathrm{H}})^{-1}\tilde{\mathbf{z}} \,. \tag{15}$$

If we define $\mathbf{S} = \mathrm{diag}(s_1, \cdots, s_K)$ and note that $\mathbf{P} = \mathbf{S}\mathbf{S}^{\mathrm{H}}$, the expression in (15) can be further rewritten as follows:

$$\begin{aligned} \hat{\mathbf{s}} &= \mathbf{S}\mathbf{S}^{\mathrm{H}}\mathbf{A}^{\mathrm{H}}(\mathbf{A}\mathbf{S}\mathbf{S}^{\mathrm{H}}\mathbf{A}^{\mathrm{H}})^{-1}\tilde{\mathbf{z}} \\ &= \mathbf{S}(\mathbf{A}\mathbf{S})^{\mathrm{H}}[(\mathbf{A}\mathbf{S})(\mathbf{A}\mathbf{S})^{\mathrm{H}}]^{-1}\tilde{\mathbf{z}} \\ &= \mathbf{S}(\mathbf{A}\mathbf{S})^{+}\tilde{\mathbf{z}}, \end{aligned} \tag{16}$$

where $(\mathbf{A}\mathbf{S})^{+}$ denotes the Moore-Penrose inverse. We note from this expression that, interestingly enough, the SPOC algorithm is mathematically identical to the basic form of FOCUSS [9]. In [11], a generalized version of FOCUSS is proposed, which includes a sparsity parameter p and a regularization parameter λ. We note that this generalized form reduces to the basic form when $p = 0$ and $\lambda = 0$. In addition, in [10], it is shown that these two parameters in the generalized FOCUSS affect the performance of the algorithm significantly, and the tuning of these parameters is difficult in practice, especially when the problem dimensions become large. From this knowledge on the performance of FOCUSS, we can infer about the performance of SPOC. Regarding the computational complexities, SPOC in (10) (only the second term is updated in each iteration) has a complexity of $O(K^2 + N^2K)$, while FOCUSS in (15) $O(N^2K)$, for $K \gg N$. Hence FOCUSS is computationally more efficient than SPOC.

B. Minimum Variance Distortionless Response (MVDR)

The MVDR algorithm requires the knowledge of the array covariance matrix, which is usually replaced by the sample covariance matrix in practice when multiple snapshots (pings) are available. However, in our application, the environment is constantly changing and hence only a single snapshot is available. In this case, the sample covariance matrix can be constructed using spatial smoothing, which simply divides the entire hydrophone array into overlapping subarrays and takes the outputs from these subarrays as individual snapshots. Specifically, the N-element ULA is divided into J overlapping subarrays, each containing $\tilde{N}$ sensors, with two adjacent subarrays separated from each other by L sensors, where $(J-1)L+\tilde{N} \leq N$. In this way, the original single snapshot of length N is divided into J shorter snapshots, each of length $\tilde{N}$. Clearly, spatial smoothing is suboptimal and trades off angular resolution for snapshots. Moreover, it can only work for ULA.

Following the discussion above, the sample covariance matrix is given by:

$$\tilde{\mathbf{R}} = \tilde{\mathbf{Z}}\tilde{\mathbf{Z}}^{\mathrm{H}}, \tag{17}$$

where $\tilde{\mathbf{Z}}$ represents the data matrix obtained by spatial smoothing. For forward spatial smoothing, $\tilde{\mathbf{Z}}$ is given by:

$$\tilde{\mathbf{Z}} = \begin{bmatrix} \tilde{z}_1 & \tilde{z}_{L+1} & \cdots & \tilde{z}_{(J-1)L+1} \\ \tilde{z}_2 & \tilde{z}_{L+2} & \cdots & \tilde{z}_{(J-1)L+2} \\ \vdots & \vdots & \ddots & \vdots \\ \tilde{z}_{\tilde{N}} & \tilde{z}_{L+\tilde{N}} & \cdots & \tilde{z}_{(J-1)L+\tilde{N}} \end{bmatrix}. \tag{18}$$

For backward spatial smoothing, $\tilde{\mathbf{Z}}$ is obtained by taking the complex conjugate of (18) and then flipping the resulting matrix upside down. For forward-backward spatial smoothing, $\tilde{\mathbf{Z}}$ is simply (18) concatenated with the data matrix from backward spatial smoothing [12].

Since with spatial smoothing the effective aperture of the array is reduced to $\tilde{N}$, the definition of the steering vector has to be modified accordingly. For the sake of notational simplicity and consistency, we still use $\mathbf{a}_k$, which is redefined as $\mathbf{a}_k = [1, e^{j\tilde{\phi}_k}, \cdots, e^{j(\tilde{N}-1)\tilde{\phi}_k}]^{\mathrm{T}}$ to account for the aperture length change, to denote the steering vector associated with the angular grid point k. The proper definition should be clear from the context and should not cause any confusion to the reader. With the notations defined above, the angular spectral estimate at $\tilde{\theta}_k$ using MVDR is given by [13]:

$$|\hat{s}_k|^2 = \frac{1}{\mathbf{a}_k^{\mathrm{H}}\tilde{\mathbf{R}}^{-1}\mathbf{a}_k}, \qquad 1 \leq k \leq K\,. \tag{19}$$

C. Iterative Adaptive Approach (IAA)

In this subsection, we introduce the Iterative Adaptive Approach (IAA) [10]. The IAA algorithm has been shown to possess superior performance over many existing algorithms in several applications such as source localization [10] and MIMO radar imaging [14], etc. We first give the original form of the IAA algorithm, and then discuss various issues pertaining to the implementation of the algorithm, namely regularizations and computational complexities.

1) The original IAA algorithm: IAA is a nonparametric adaptive algorithm recently proposed for array processing applications. The IAA algorithm relies on iteratively solving a weighted least squares (WLS) problem. As before, let $\mathbf{P}$ denote the $K \times K$ diagonal matrix whose diagonal contains the power at each angular grid point, and furthermore, define the interference (targets at angles other than the angle of current interest $\tilde{\theta}_k$) and noise covariance matrix $\mathbf{Q}_k$ to be:

$$\mathbf{Q}_k = \mathbf{R} - |s_k|^2\mathbf{a}_k\mathbf{a}_k^{\mathrm{H}}, \tag{20}$$

where $\mathbf{R} = \mathbf{A}\mathbf{P}\mathbf{A}^{\mathrm{H}}$. Using these notations, the WLS cost function is given by:

$$||\tilde{\mathbf{z}} - s_k\mathbf{a}_k||^2_{\mathbf{Q}_k^{-1}}, \tag{21}$$

where $||\mathbf{x}||^2_{\mathbf{Q}_k^{-1}} \triangleq \mathbf{x}^{\mathrm{H}}\mathbf{Q}_k^{-1}\mathbf{x}$. The minimization of (21) with respect to s_k gives:

$$\hat{s}_k = \frac{\mathbf{a}_k^{\mathrm{H}}\mathbf{Q}_k^{-1}\tilde{\mathbf{z}}}{\mathbf{a}_k^{\mathrm{H}}\mathbf{Q}_k^{-1}\mathbf{a}_k}\,. \tag{22}$$

Using the definition of $\mathbf{Q}_k$ and the matrix inversion lemma, (22) can be writtern as:

$$\hat{s}_k = \frac{\mathbf{a}_k^{\mathrm{H}}\mathbf{R}^{-1}\tilde{\mathbf{z}}}{\mathbf{a}_k^{\mathrm{H}}\mathbf{R}^{-1}\mathbf{a}_k}\,. \tag{23}$$

This avoids the construction of $\mathbf{Q}_k$ for each angular grid point k, and thus substantially saves computation time. Once $\mathbf{R}$ is computed, the computation of $\hat{s}_k$, for $1 \leq k \leq K$, will be independent of each other, and hence IAA is amenable to parallel implementation. Since (23) requires $\mathbf{R}$, which in turn depends on the unknown target powers, IAA has to be implemented in an iterative manner. Usually, IAA is initialized

TABLE I

ITERATIVE ADAPTIVE APPROACH (IAA)

Initialization
Set $\mathbf{R}^{(0)} = \mathbf{I}$ in (23) and compute the initial values of $\hat{s}_k$, for $1 \leq k \leq K$. This is equivalent to the CBF.
Iteration
At the i^{th} iteration, the estimate of s_k is given by: $\hat{s}_k^{(i)} = \frac{\mathbf{a}_k^{\text{H}}(\mathbf{R}^{(i)})^{-1}\tilde{\mathbf{z}}}{\mathbf{a}_k^{\text{H}}(\mathbf{R}^{(i)})^{-1}\mathbf{a}_k}$ where $\mathbf{R}^{(i)} = \sum_{k=1}^{K} \lvert\hat{s}_k^{(i-1)}\rvert^2 \mathbf{a}_k \mathbf{a}_k^{\text{H}}$.
Termination
The iteration is terminated when the relative change $\lvert\hat{s}_k^{(i)} - \hat{s}_k^{(i-1)}\rvert^2$ is less than a specified tolerance. Our experience is that IAA does not provide significant improvement in performance after about 10 iterations.

TABLE II

RANGE-SELECTIVE IAA (RSIAA)

Initialization
Set $\mathbf{R}^{(0)} = \mathbf{I}$ in (23) and compute the initial values of $\hat{s}_k$, for $1 \leq k \leq K$. This is equivalent to the CBF.
Iteration
At the i^{th} iteration, the estimate of s_k is given by: $\hat{s}_k^{(i)} = \frac{\mathbf{a}_k^{\text{H}}(\mathbf{R}^{(i)})^{-1}\tilde{\mathbf{z}}}{\mathbf{a}_k^{\text{H}}(\mathbf{R}^{(i)})^{-1}\mathbf{a}_k}$ for $k \in \{\mathcal{L} \cup \mathcal{T}\}$ where $\mathbf{R}^{(i)} = \sum_{k\in\mathcal{L}} \lvert\hat{s}_k^{(i-1)}\rvert^2 \mathbf{a}_k \mathbf{a}_k^{\text{H}} + \sum_{k\in\mathcal{T}} \lvert\hat{s}_k^{(i-1)}\rvert^2 \mathbf{a}_k \mathbf{a}_k^{\text{H}}$.
Termination
The iteration is terminated when the relative change $\lvert\hat{s}_k^{(i)} - \hat{s}_k^{(i-1)}\rvert^2$, is less than a specified tolerance.

TABLE III

REGULARIZED IAA METHODS

Regularization method	**Matrix $(\mathbf{R})$**
IAA (with the knowledge of noise covariances)	$\mathbf{R}^{(i)} = \sum_{k=1}^{K} \lvert\hat{s}_k^{(i-1)}\rvert^2 \mathbf{a}_k \mathbf{a}_k^{\text{H}} + \mathbf{\Sigma}$, where $\mathbf{\Sigma}$ denotes the noise covariance matrix.
IAAR [14]	$\mathbf{R}^{(i)} = \sum_{k=1}^{K} \lvert\hat{s}_k^{(i-1)}\rvert^2 \mathbf{a}_k \mathbf{a}_k^{\text{H}} + \sum_{n=1}^{N} \lvert\hat{\gamma}_n^{(i-1)}\rvert^2 \mathbf{u}_n \mathbf{u}_n^{\text{H}}$, where $\mathbf{u}_n$ denotes the n^{th} column of the $N \times N$ identity matrix, and $\hat{\gamma}_n^{(i)} = \frac{\mathbf{u}_n^{\text{H}}(\mathbf{R}^{(i)})^{-1}\tilde{\mathbf{z}}}{\mathbf{u}_n^{\text{H}}(\mathbf{R}^{(i)})^{-1}\mathbf{u}_n}$.
VIAA [15]	$\mathbf{R}^{(i)} = \sum_{k\in\mathcal{K}^{(i-1)}} \lvert\hat{s}_k^{(i-1)}\rvert^2 \mathbf{a}_k \mathbf{a}_k^{\text{H}} + \sum_{k\in[1,K]\setminus\mathcal{K}^{(i-1)}} \lvert\hat{s}_k^{(i-1)}\rvert^2 \mathbf{I}$, where $\mathcal{K}^{(i-1)}$ denotes the subset of $[1, K]$ containing the indices corresponding to the N largest values of $\{\lvert\hat{s}_k^{(i-1)}\rvert^2\}$ and $\mathbf{I}$ denotes the $N \times N$ identity matrix.

by the CBF. The angular spectral estimate at $\tilde{\theta}_k$ using IAA is equal to the squared magnitude of $\hat{s}_k$ given by (23). The steps of the IAA algorithm are summarized in Table I.

2) Time complexity and computationally efficient IAA algorithm: In each iteration of the IAA algorithm, the construction of the $\mathbf{R}$ matrix, formed as a sum of K rank-one matrices, requires $O(KN^2)$ flops. Then the inversion of $\mathbf{R}$, done once for each iteration, requires $O(N^3)$. A major computational requirement in each iteration comes from the calculation of $\hat{s}_k$, which requires a matrix-vector multiplication $\mathbf{R}^{-1}\mathbf{a}_k$. Each of these matrix-vector multiplications requires $O(N^2)$ and thus the calculation of all estimates $\{\hat{s}_k\}_{k=1}^K$ requires $O(KN^2)$. Therefore in each iteration, IAA requires $O(KN^2 + N^3)$. Since the number of iterations is usually quite small (the performance of IAA does not change significantly after 15 iterations), it follows that $O(KN^2 + N^3)$ is the total complexity of the IAA algorithm.

From the analysis above, we see that the IAA method can be computationally expensive when the angular grid size is large. However, if we are only interested in part of the spectrum that is over a certain range of angles (or a subset of the grid points), the computations can be reduced drastically by using the range-selective IAA (RSIAA) algorithm. In RSIAA, all the angular spectral components in the range of (angles of) interest (ROI) but only the N largest angular spectral components from the region outside ROI are used in the construction of $\mathbf{R}$. Let $\mathcal{L} \subset [1, K]$ denote the grid points in ROI, and let $\mathcal{T} \in \{[1, K]\setminus \mathcal{L}\}$ denote the indices of the N largest values of the initial DAS spectrum in the region outside ROI. Table II summarizes the RSIAA algorithm. In the experimental examples presented below, only the original IAA is used since the array size used in the experiment is modest.

3) Regularizations of the IAA algorithm: The matrix $\mathbf{R}$ in (23) may become ill-conditioned as the iteration proceeds. In this case, we need certain regularizations so that IAA can work properly. The various regularization methods differ only in the construction of the $\mathbf{R}$ matrix. At the i^{th} iteration, the $\mathbf{R}$ matrix for each regularization method is constructed using the expression shown in Table III.

In certain applications, information about the noise covariance matrix is available, which can be used as a regularization term. In other cases when this information is unavailable, we can simply use a scaled identity matrix if the noise terms associated with all sensors are independently and identically distributed (i.i.d.) Gaussian random variables. In the case of IAAR, at convergence the values $\{\lvert\hat{\gamma}_n\rvert^2\}_{n=1}^N$ will be close to the noise variances. The regularization in VIAA is based on the intuitive fact that from N data samples we can reliably estimate no more than N values in the angular spectrum. Thus the N largest values in the spectrum are used to construct the signal part of $\mathbf{R}$ and the sum of the remaining values in the spectrum is taken as an estimate of the noise floor.

IV. Experimental Results

In the experiment, a rail was deployed at Sydney harbor, Australia, in an area with a sandy bottom. The water depth was about 6 m. The rail was 20 m long and 4 m above the sea floor. There were slight swell and small ripples in the sea. A wide-band sonar system, consisting of a projector and a 32-element linear hydrophone array, was mounted on a motorized trolley that moved uniformly along the rail during sonar transmission and reception. The speed of the trolley was much smaller than the underwater sound speed, so that the sonar position could be assumed constant during a single ping but varied from ping to ping. The transmitter was located at the array center and the hydrophones were uniformly spaced at 0.83 cm. The projector emitted an acoustic beam, in the broadside direction of the array, onto the sea floor. The beam was wide in azimuth to provide large area coverage, but narrow in elevation with low sidelobes to minimize multipath interference and sea surface reverberation. The beam was properly tilted in the vertical plane to cover a range swath from 50 m to over 120 m. Linear frequency-modulated pulses, each of 4 ms in duration, with a center frequency of 150 kHz and a bandwidth of 64 kHz, were used in the experiment. The target field consisted of a number of man-made objects located on the sandy sea floor at a range of 60-120 m from the center of the rail. The hydrophone outputs were sampled at a frequency of 560 kHz. The digitized signals were matched filtered, converted into baseband, and decimated by a factor of eight prior to beamforming. The range grid size is therefore determined to be $\frac{1560\text{m/s}}{2\times(560\text{kHz}/8)} = 0.011\text{m}$. Data recorded for various pings (or sonar positions) were processed using all three adaptive algorithms (SPOC, MVDR and IAA) as well as the CBF algorithm. The original form of IAA was used. For the adaptive algorithms, the cubic interpolation method [7] was used in the spatial resampling step to obtain $\tilde{Z}_n(f)$ from the available samples $Z_n(f)$. For the MVDR algorithm, forward-backward spatial smoothing was performed with $\tilde{N} = 16$, $L = 1$ and $J = 17$. The number of iterations used in both SPOC and IAA algorithms was 10. The CBF was implemented in the frequency domain using the fast Fourier transform (FFT) (More specifically, the time series from each sensor was transformed into the frequency domain using the FFT. For each frequency bin, the spectral data from the N sensors were linearly combined, without shading, after being appropriately phase-shifted. The resulting beamformed data were then transformed back into the time domain using the inverse FFT.). For a fair comparison of the different beamforming algorithms, all angular spectra were computed at the same set of angular grid points $\{\tilde{\theta}_k : 1 \leq k \leq 1801\}$, which were uniformly spaced over $(-90°, 90°)$. Typical results are presented here for illustration.

Figure 2 shows the sonar images of an area containing two exercise mines and a cylinder, produced using the adaptive beamformers as well as the CBF algorithm, for a particular ping. The cylinder was a thin metallic shell filled with fresh water. In Figure 2, each object occupies a number of image pixels. The intensity of each image in Figure 2 is normalized, expressed in decibels, to peak at 0 dB and clipped at -40 dB. Several observations are in order based on the images shown. First, bright horizontal lines (caused by the sidelobes of the beamformer) appear in the CBF image. These artifacts extend over a smaller angular region in the MVDR, and are minimal in the IAA image and absent in the SPOC image. Second, strong scattering centers (acoustic highlights) are clearly observed for each object in the images produced by CBF, IAA and MVDR. However, they are not so obvious in the SPOC image unless it is zoomed in to examine its fine details. Thus the objects are more difficult to detect visually in the SPOC image than in the other three images. Third, a zoom-in view of the SPOC image shows that each object appears acoustically as a collection of sparse discrete points with a few of them being dominant, which is a distorted representation of the imaged object having a smooth surface. In contrast to the "sparse" nature of the SPOC image, the IAA image is similar to the CBF and MVDR images in that all three are "dense" in nature (i.e., each object in the image is represented by a set of densely populated points). Another observation which is evident from Figure 2 is that the adaptive beamformers provide higher angular resolution than the CBF as indicated by their narrower main lobes [6]. The angular resolution of IAA is better than that of MVDR. Therefore, it can be concluded that IAA produces the best image from the perspective of visual inspection (minimal artifacts, clear acoustic highlights, high density and good resolution).

To further illustrate the superior performance of IAA over the other algorithms, Figures 3 and 4 show, respectively, the sonar images of two other areas, one containing a 20-m-long linear array and the other a beer keg, produced using the adaptive beamformers and the CBF. The intensity of each image in Figures 3 and 4 is normalized, expressed in decibels, to peak at 0 dB and clipped at -40 dB. As is evidenced from these images, IAA produces images with minimal artifacts, clear acoustic highlights of the object, a high density of pixels representing the object, and a good angular resolution.

V. Conclusion

We have considered the wide-band active sonar imaging problem for the detection and identification of man-made objects located on the sea floor. The conventional beamforming algorithm produces sonar images with low angular resolution and high sidelobe levels. The adaptive beamforming algorithms have the potential of producing better images than CBF in terms of sidelobe suppression and angular resolution. Prior to the application of narrow-band adaptive beamforming algorithms to a wide-band active sonar, spatial resampling is required on the received signal at each hydrophone output. The SPOC algorithm was shown to be identical to the basic form of the FOCUSS algorithm, which enables the evaluation of the former based on the knowledge of the performance of the latter. A new adaptive algorithm, called IAA, was introduced for the sonar application and its various implementation

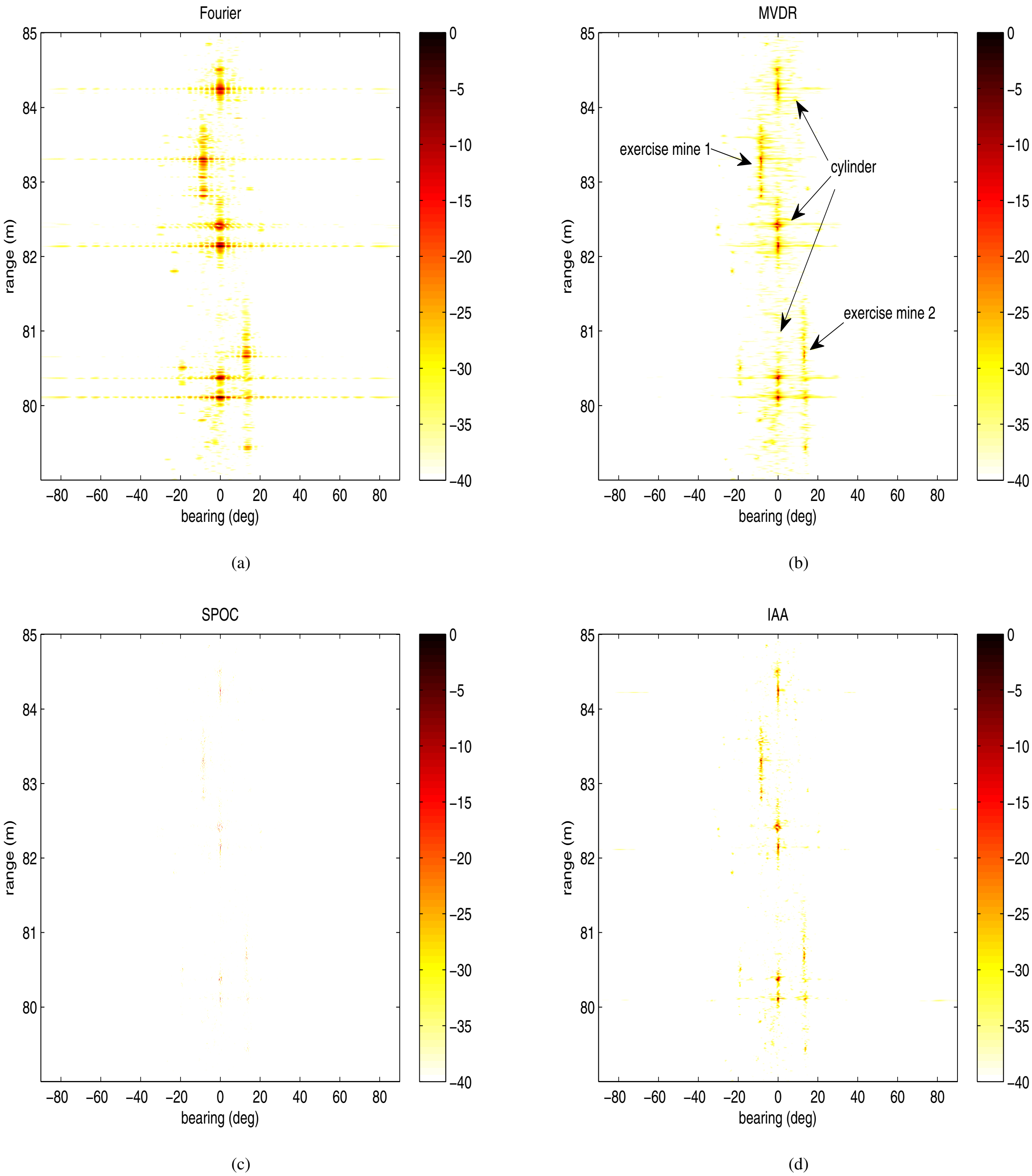

Fig. 2. Sonar images of an area containing two exercise mines and a cylinder, produced by using (a) CBF, (b) MVDR, (c) SPOC, and (d) IAA beamformers. The image intensity is normalized, expressed in decibels, to peak at 0 dB and clipped at -40 dB.

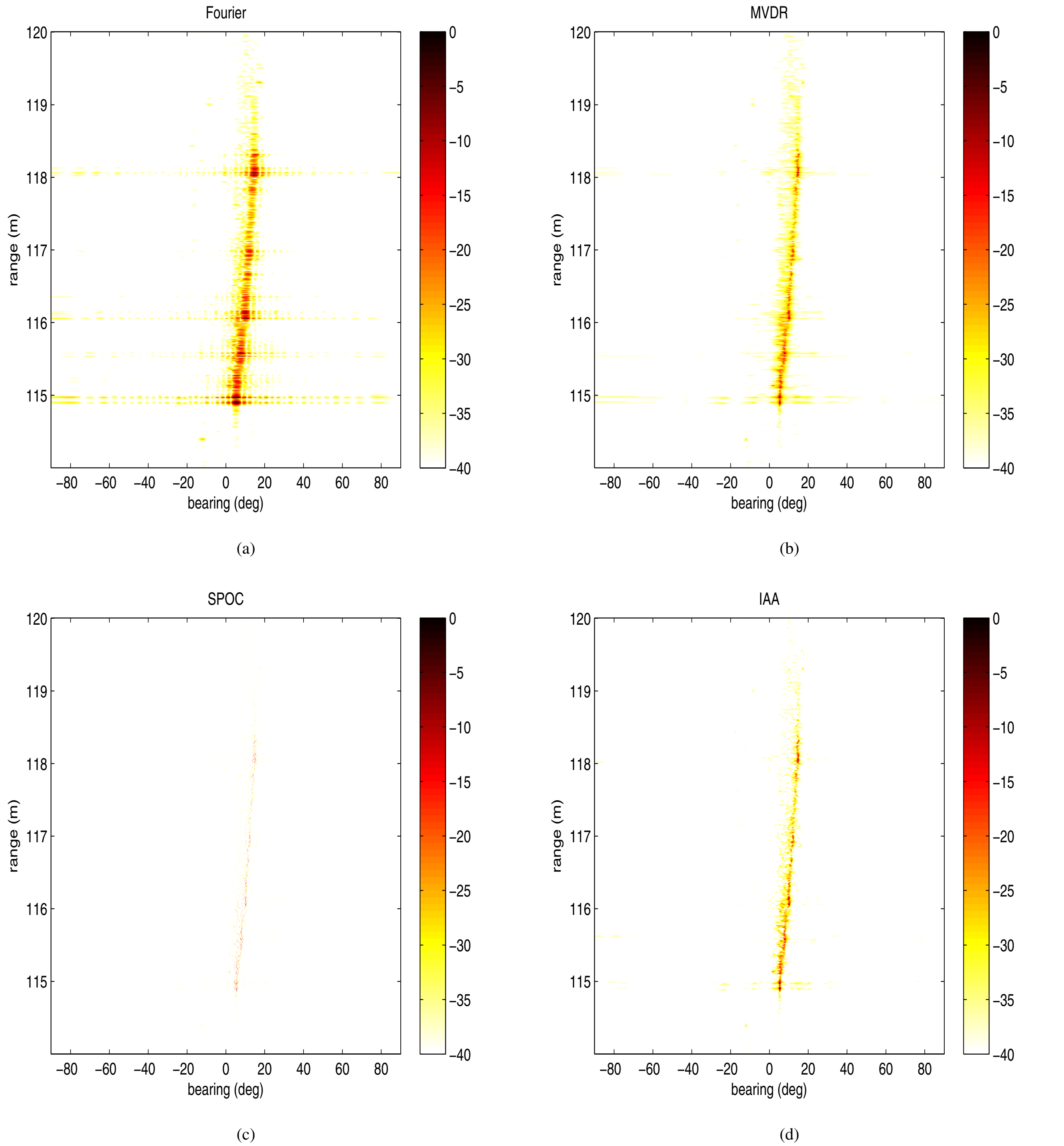

Fig. 3. Sonar images of an area containing a 20-m-long linear hydrophone array, produced by using (a) CBF, (b) MVDR, (c) SPOC, and (d) IAA beamformers. The image intensity is normalized, expressed in decibels, to peak at 0 dB and clipped at -40 dB.

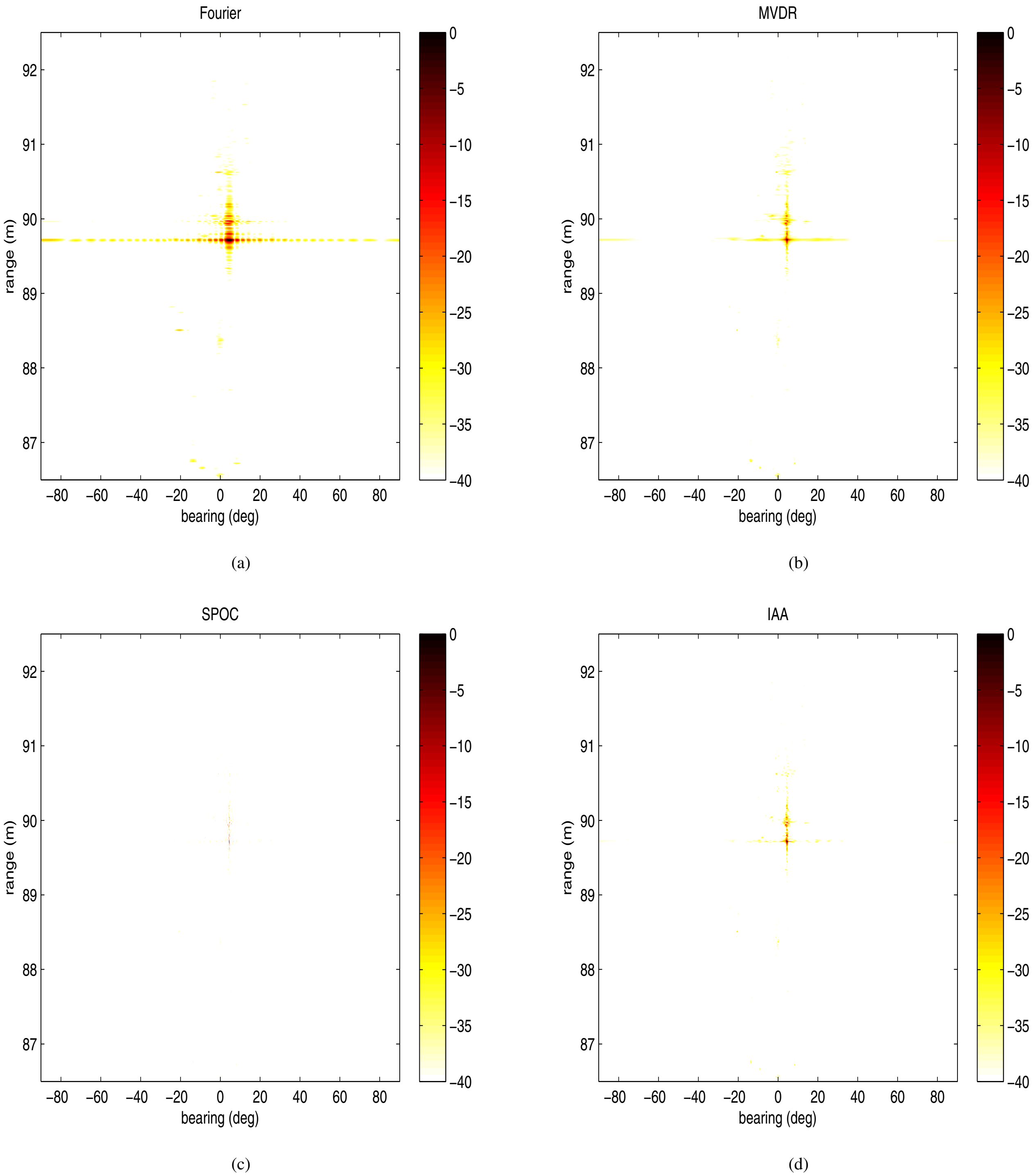

Fig. 4. Sonar images of an area containing a beer keg, produced by using (a) CBF, (b) MVDR, (c) SPOC, and (d) IAA beamformers. The image intensity is normalized, expressed in decibels, to peak at 0 dB and clipped at -40 dB.

aspects were discussed. We have evaluated the three adaptive algorithms: SPOC, MVDR and IAA using real sonar data. Experimental results show the superior performance of IAA over the CBF and the other two adaptive algorithms (MVDR and SPOC). Sonar images generated with IAA have minimal artifacts, clear acoustic highlights of the imaged object, a high density of pixels representing the imaged object, and a good angular resolution.

ACKNOWLEDGMENT

This work was supported in part by the Office of Naval Research (ONR) under grants No. N00014-09-1-0211. The measurements of the object field were made using an underwater rail and sonar provided by DERA (UK) for a joint experiment conducted under the auspices of TTCP MAR TP-13 in Sydney Harbour.

REFERENCES

[1] M. Chantler, D. Lane, D. Dai, and N. Williams, "Detection and tracking of returns in sector-scan sonar image sequences," *IEE Proceedings of Radar, Sonar and Navigation*, vol. 143, no. 3, June 1996.

[2] M. Chantler and J. Stoner, "Automatic interpretation of sonar image sequences using temporal feature measures," *IEEE Journal of Oceanic Engineering*, vol. 22, no. 1, January 1997.

[3] I. Ruiz, D. Lane, and M. Chantler, "A comparison of inter-frame feature measures for robust object classification in sector scan sonar image sequences," *IEEE Journal of Oceanic Engineering*, vol. 24, no. 4, October 1999.

[4] S. Perry and L. Guan, "Detection of small man-made objects in sector scan imagery using neural networks," *Proceedings of OCEANS'01*, vol. 4, pp. 2108–2114, 2001.

[5] ——, "Pulse-length-tolerant features and detectors for sector-scan sonar imagery," *IEEE Journal of Oceanic Engineering*, vol. 29, no. 1, January 2004.

[6] K. W. Lo, "Adaptive array processing for wide-band active sonars," *IEEE Journal of Oceanic Engineering*, vol. 29, no. 3, pp. 837–846, July 2004.

[7] J. Krolik and D. Swingler, "Focused wide-band array processing by spatial resampling," *IEEE Transactions on Acoustics, Speech, and Signal Processing*, vol. 38, no. 2, pp. 356–360, February 1990.

[8] R. Bethel, B. Shapo, and H. V. Trees, "Single Snapshot Spatial Processing: Optimized and Constrained," *Sensor Array and Multichannel Signal Processing Workshop Proceedings*, pp. 508–512, 2002.

[9] I. F. Gorodnitsky and B. D. Rao, "Sparse signal reconstruction from limited data using FOCUSS: A re-weighted minimum norm algorithm," *IEEE Transactions on Signal Processing*, vol. 45, no. 3, pp. 600–616, 1997.

[10] T. Yardibi, J. Li, P. Stoica, M. Xue, and A. B. Baggeroer, "Source localization and sensing: A nonparametric iterative adaptive approach based on weighted least squares," to appear in *IEEE Transactions on Aerospace and Elecctronic Systems*, 2009, available: http://www.sal.ufl.edu/eel6935/2008/IAA.pdf.

[11] S. F. Cotter, B. D. Rao, E. Kjersti, and K. Kreutz-Delgado, "Sparse solutions to linear inverse problems with multiple measurement vectors," *IEEE Transactions on Signal Processing*, vol. 53, no. 7, pp. 2477–2488, 2005.

[12] S. U. Pillai, *Array Signal Processing*. New York, NY: Springer-Verlag New York Inc., 1989.

[13] P. Stoica and R. L. Moses, *Spectral Analysis of Signals*. Upper Saddle River, NJ: Prentice-Hall, 2005.

[14] W. Roberts, P. Stoica, J. Li, T. Yardibi, , and F. Sadjadi, "Iterative adaptive approaches to MIMO radar imaging," to appear in *IEEE Journal of Selected Topics in Signal Processing*, available: http://www.sal.ufl.edu/papers/MIMOIAA.pdf.

[15] Z. Chen, P. Babu, P. Stoica, and J. Li, "Optimally tapered periodograms for nonuniformly sampled data," submitted in *IET Signal Processing*, 2009, available: http://www.sal.ufl.edu/papers/OptTaper.pdf.